Research Article | Vol. 24, No. 18 | 5 Sep 2016 | OPTICS EXPRESS 20472

Optics EXPRESS

All-metal structural color printing based on aluminum plasmonic metasurfaces

ZHIGANG LI,[1,3] WEI WANG,[1,3] DANIEL ROSENMANN,[2] DAVID A. CZAPLEWSKI,[2] XIAODONG YANG,[1,4] AND JIE GAO[1,*]

[1]*Department of Mechanical and Aerospace Engineering, Missouri University of Science and Technology, Rolla, MO 65409, USA*
[2]*Center for Nanoscale Materials, Argonne National Laboratory, Argonne, IL 60439, USA*
[3]*These authors contributed equally to this work*
[4]*yangxia@mst.edu*
[*]*gaojie@mst.edu*

Abstract: An all-metal structural color printing platform based on aluminum plasmonic metasurfaces is proposed and demonstrated with high color performance using only one-step etching process on aluminum surface. A wide visible color range is realized with the designed metallic square-shaped disk arrays by simply adjusting geometrical parameters of the disk etching depth, disk width and unit cell period. The demonstrated all-metal microscale structural color printing on aluminum surface offers great potential for many practical color related applications.

OCIS codes: (050.6624) Subwavelength structures; (240.6680) Surface plasmons; (160.3918) Metamaterials; (330.1690) Color.

References and links

1. K. Nassau, "The physics and chemistry of color: The 15 mechanisms," in *The Science of Color*, 2nd ed. (2003), pp. 247–280.
2. H. Park, Y. Dan, K. Seo, Y. J. Yu, P. K. Duane, M. Wober, and K. B. Crozier, "Filter-free image sensor pixels comprising silicon nanowires with selective color absorption," Nano Lett. **14**(4), 1804–1809 (2014).
3. K. Seo, M. Wober, P. Steinvurzel, E. Schonbrun, Y. Dan, T. Ellenbogen, and K. B. Crozier, "Multicolored vertical silicon nanowires," Nano Lett. **11**(4), 1851–1856 (2011).
4. L. Huang, X. Chen, H. Mühlenbernd, H. Zhang, S. Chen, B. Bai, Q. Tan, G. Jin, K.-W. Cheah, C.-W. Qiu, J. Li, T. Zentgraf, and S. Zhang, "Three-dimensional optical holography using a plasmonic metasurface," Nat. Commun. **4**, 2808 (2013).
5. A. Poddubny, I. Iorsh, P. Belov, and Y. Kivshar, "Hyperbolic metamaterials," Nat. Photonics **7**(12), 948–957 (2013).
6. N. Meinzer, W. L. Barnes, and I. R. Hooper, "Plasmonic meta-atoms and metasurfaces," Nat. Photonics **8**(12), 889–898 (2014).
7. N. Yu and F. Capasso, "Flat optics with designer metasurfaces," Nat. Mater. **13**(2), 139–150 (2014).
8. J. A. Schuller, E. S. Barnard, W. Cai, Y. C. Jun, J. S. White, and M. L. Brongersma, "Plasmonics for extreme light concentration and manipulation," Nat. Mater. **9**(3), 193–204 (2010).
9. H. J. Park, T. Xu, J. Y. Lee, A. Ledbetter, and L. J. Guo, "Photonic color filters integrated with organic solar cells for energy harvesting," ACS Nano **5**(9), 7055–7060 (2011).
10. B. Zeng, Y. Gao, and F. J. Bartoli, "Ultrathin nanostructured metals for highly transmissive plasmonic subtractive color filters," Sci. Rep. **3**, 2840 (2013).
11. M. J. Uddin, T. Khaleque, and R. Magnusson, "Guided-mode resonant polarization-controlled tunable color filters," Opt. Express **22**(10), 12307–12315 (2014).
12. C. Genet and T. W. Ebbesen, "Light in tiny holes," Nature **445**(7123), 39–46 (2007).
13. Q. Chen and D. R. S. Cumming, "High transmission and low color cross-talk plasmonic color filters using triangular-lattice hole arrays in aluminum films," Opt. Express **18**(13), 14056–14062 (2010).
14. D. Inoue, A. Miura, T. Nomura, H. Fujikawa, K. Sato, N. Ikeda, D. Tsuya, Y. Sugimoto, and Y. Koide, "Polarization independent visible color filter comprising an aluminum film with surface-plasmon enhanced transmission through a subwavelength array of holes," Appl. Phys. Lett. **98**(9), 093113 (2011).
15. S. Yokogawa, S. P. Burgos, and H. A. Atwater, "Plasmonic color filters for CMOS image sensor applications," Nano Lett. **12**(8), 4349–4354 (2012).
16. Z. Li, A. W. Clark, and J. M. Cooper, "Dual color plasmonic pixels create a polarization controlled nano color palette," ACS Nano **10**(1), 492–498 (2016).

#268905 http://dx.doi.org/10.1364/OE.24.020472
Journal © 2016 Received 20 Jun 2016; revised 21 Jul 2016; accepted 9 Aug 2016; published 26 Aug 2016

Optics EXPRESS

17. T. Ellenbogen, K. Seo, and K. B. Crozier, "Chromatic plasmonic polarizers for active visible color filtering and polarimetry," Nano Lett. **12**(2), 1026–1031 (2012).
18. G. Si, Y. Zhao, J. Lv, M. Lu, F. Wang, H. Liu, N. Xiang, T. J. Huang, A. J. Danner, J. Teng, and Y. J. Liu, "Reflective plasmonic color filters based on lithographically patterned silver nanorod arrays," Nanoscale **5**(14), 6243–6248 (2013).
19. J. Do, M. Fedoruk, F. Jäckel, and J. Feldmann, "Two-color laser printing of individual gold nanorods," Nano Lett. **13**(9), 4164–4168 (2013).
20. J. S. Clausen, E. Højlund-Nielsen, A. B. Christiansen, S. Yazdi, M. Grajower, H. Taha, U. Levy, A. Kristensen, and N. A. Mortensen, "Plasmonic metasurfaces for coloration of plastic consumer products," Nano Lett. **14**(8), 4499–4504 (2014).
21. C. Saeidi and D. van der Weide, "Bandwidth-tunable optical spatial filters with nanoparticle arrays," Opt. Express **22**(10), 12499–12504 (2014).
22. T. Xu, Y.-K. Wu, X. Luo, and L. J. Guo, "Plasmonic nanoresonators for high-resolution colour filtering and spectral imaging," Nat. Commun. **1**(5), 59 (2010).
23. A. F. Kaplan, T. Xu, and L. Jay Guo, "High efficiency resonance-based spectrum filters with tunable transmission bandwidth fabricated using nanoimprint lithography," Appl. Phys. Lett. **99**(14), 143111 (2011).
24. A. S. Roberts, A. Pors, O. Albrektsen, and S. I. Bozhevolnyi, "Subwavelength plasmonic color printing protected for ambient use," Nano Lett. **14**(2), 783–787 (2014).
25. F. Cheng, J. Gao, T. S. Luk, and X. Yang, "Structural color printing based on plasmonic metasurfaces of perfect light absorption," Sci. Rep. **5**, 11045 (2015).
26. F. Cheng, J. Gao, L. Stan, D. Rosenmann, D. Czaplewski, and X. Yang, "Aluminum plasmonic metamaterials for structural color printing," Opt. Express **23**(11), 14552–14560 (2015).
27. F. Cheng, X. Yang, D. Rosenmann, L. Stan, D. Czaplewski, and J. Gao, "Enhanced structural color generation in aluminum metamaterials coated with a thin polymer layer," Opt. Express **23**(19), 25329–25339 (2015).
28. K. Kumar, H. Duan, R. S. Hegde, S. C. W. Koh, J. N. Wei, and J. K. W. Yang, "Printing colour at the optical diffraction limit," Nat. Nanotechnol. **7**(9), 557–561 (2012).
29. X. M. Goh, Y. Zheng, S. J. Tan, L. Zhang, K. Kumar, C.-W. Qiu, and J. K. W. Yang, "Three-dimensional plasmonic stereoscopic prints in full colour," Nat. Commun. **5**, 5361 (2014).
30. S. J. Tan, L. Zhang, D. Zhu, X. M. Goh, Y. M. Wang, K. Kumar, C. W. Qiu, and J. K. W. Yang, "Plasmonic color palettes for photorealistic printing with aluminum nanostructures," Nano Lett. **14**(7), 4023–4029 (2014).
31. C. L. Haynes, A. D. McFarland, L. L. Zhao, R. P. Van Duyne, G. C. Schatz, L. Gunnarsson, J. Prikulis, B. Kasemo, and M. Käll, "Nanoparticle optics: The importance of radiative dipole coupling in two-dimensional nanoparticle arrays," J. Phys. Chem. B **107**(30), 7337–7342 (2003).
32. S. Zou and G. C. Schatz, "Theoretical studies of plasmon resonances in one-dimensional nanoparticle chains: narrow lineshapes with tunable widths," Nanotechnology **17**(11), 2813–2820 (2006).
33. V. A. Markel and A. K. Sarychev, "Propagation of surface plasmons in ordered and disordered chains of metal nanospheres," Phys. Rev. B **75**(8), 085426 (2007).
34. Y.-K. R. Wu, A. E. Hollowell, C. Zhang, and L. J. Guo, "Angle-insensitive structural colours based on metallic nanocavities and coloured pixels beyond the diffraction limit," Sci. Rep. **3**, 1194 (2013).
35. T. W. Ebbesen, H. J. Lezec, H. F. Ghaemi, T. Thio, P. A. Wolff, T. Thio, and P. A. Wolff, "Extraordinary optical transmission through sub-wavelength hole arrays," Nature **86**, 1114–1117 (1998).
36. L. Martín-Moreno, F. J. García-Vidal, H. J. Lezec, K. M. Pellerin, T. Thio, J. B. Pendry, and T. W. Ebbesen, "Theory of extraordinary optical transmission through subwavelength hole arrays," Phys. Rev. Lett. **86**(6), 1114–1117 (2001).
37. H. Liu and P. Lalanne, "Microscopic theory of the extraordinary optical transmission," Nature **452**(7188), 728–731 (2008).
38. R. J. H. Ng, X. M. Goh, and J. K. W. Yang, "All-metal nanostructured substrates as subtractive color reflectors with near-perfect absorptance," Opt. Express **23**(25), 32597–32605 (2015).
39. J. Zhang, J.-Y. Ou, N. Papasimakis, Y. Chen, K. F. Macdonald, and N. I. Zheludev, "Continuous metal plasmonic frequency selective surfaces," Opt. Express **19**(23), 23279–23285 (2011).
40. V. R. Shrestha, S. S. Lee, E. S. Kim, and D. Y. Choi, "Aluminum plasmonics based highly transmissive polarization-independent subtractive color filters exploiting a nanopatch array," Nano Lett. **14**(11), 6672–6678 (2014).
41. L. Wang, R. J. H. Ng, S. S. Dinachali, M. Jalali, Y. Yu, and J. K. W. Yang, "Large area plasmonic color palettes with expanded gamut using colloidal self-assembly," ACS Photonics **3**(4), 627–633 (2016).
42. T. Søndergaard, S. M. Novikov, T. Holmgaard, R. L. Eriksen, J. Beermann, Z. Han, K. Pedersen, and S. I. Bozhevolnyi, "Plasmonic black gold by adiabatic nanofocusing and absorption of light in ultra-sharp convex grooves," Nat. Commun. **3**, 969 (2012).
43. T. Søndergaard and S. I. Bozhevolnyi, "Theoretical analysis of plasmonic black gold: Periodic arrays of ultra-sharp grooves," New J. Phys. **15**, 013034 (2013).
44. S. Westland, C. Ripamonti, and V. Cheung, "Computing CIE tristimulus values," in *Computational Colour Science Using MATLAB*® (John Wiley and Sons, Ltd., 2012), pp. 27–47.
45. V. A. Fedotov, P. L. Mladyonov, S. L. Prosvirnin, and N. I. Zheludev, "Planar electromagnetic metamaterial with a fish scale structure," Phys. Rev. E Stat. Nonlin. Soft Matter Phys. **72**(5), 056613 (2005).

Optics EXPRESS

46. W. Cai, U. K. Chettiar, H.-K. Yuan, V. C. de Silva, A. V. Kildishev, V. P. Drachev, and V. M. Shalaev, "Metamagnetics with rainbow colors," Opt. Express **15**(6), 3333–3341 (2007).
47. Z. Fang, Y.-R. Zhen, L. Fan, X. Zhu, and P. Nordlander, "Tunable wide-angle plasmonic perfect absorber at visible frequencies," Phys. Rev. B **85**(24), 1–7 (2012).
48. T. Xu, H. Shi, Y. K. Wu, A. F. Kaplan, J. G. Ok, and L. J. Guo, "Structural colors: From plasmonic to carbon nanostructures," Small **7**(22), 3128–3136 (2011).

1. Introduction

Over the past decade, different kinds of structural color filtering and printing techniques have been used to reproduce vivid colors in nature with great advantages over conventional colorant-based pigmentation [1–3]. In particular, plasmonic metamaterials and metasurfaces are receiving more attention for the next generation structural color applications due to their capability of controlling the light intensity, phase and polarization effectively [4–8]. Plasmonic nanostructures with various geometries have been developed for structural color generation with high resolution including one dimensional gratings [9–11], hole arrays [12–16], nanoantenna arrays [17–21], metal-insulator-metal (MIM) structures [10, 22–27], and combined nanodisk and nanohole arrays [28–30]. By tuning the geometries and dimensions of the plasmonic nanostructures, optical resonances in the visible frequency range can be achieved based on the mechanisms of propagating surface plasmons (SP) [12–16], localized surface plasmon resonances (LSPR) [18, 28–33], as well as Fabry-Pérot cavity modes [34]. Plasmonic color generation has been widely studied in realizing highly saturated color with narrow bandwidth [23, 25–27], color filtering with extraordinary optical transmission [35–37], high-resolution color pixels for imaging [10, 28, 34], polarization dependent [16, 17] or independent [18, 20, 21] color filtering and imaging, and angle-insensitive structural color printing [21, 34]. Noble metals like gold and silver have been traditionally employed in the color filtering and imaging platforms due to their lower ohmic losses within the visible spectrum [10,18,24,25,28,34,38]. However, the interband transition of gold limits the color range obtainable to below the wavelength of 550 nm [24,39], while silver is susceptible to oxidation and sulphidation which leads to the degradation of colors under ambient usage [18]. Consequently, a suitable substitute for noble metals, aluminum, has been highly attractive for structural color printing application due to its excellent optical response in the visible spectrum, chemical and thermal stability thanks to its natively formed oxidation layer, low cost, and complementary metal oxide semiconductor (CMOS) compatibility [15, 16, 20, 26, 27, 40]. Recently, aluminum based metamaterials with complex nanostructures such as MIM structures [10, 22–27] and combined nanodisk and nanohole arrays [28–30] have been designed to exhibit excellent color performance, however, the fabrication processes are still sophisticated, which will not only increase the production cost but degrade the color performance due to fabrication imperfections.

In this work, we introduce and demonstrate an all-metal structural color printing platform based on aluminum plasmonic metasurfaces with high color performance using a simple, one-step focused ion beam milling process on aluminum surface. By adjusting the geometrical parameters of the designed aluminum square-shaped disk arrays, including the disk etching depth, disk width and unit cell period, a wide visible color range can be realized. The mechanism of structural color generation in aluminum square-shaped disk arrays is analyzed according to the excitation of electric dipole and magnetic dipole resonances. Furthermore, the polarization and incident angle dependent optical properties of the color printing platform have also been studied. The demonstrated all-metal structural color printing on aluminum surface offers great potential for many relevant applications such as microscale imaging, information storage, and security marking.

2. Device design and fabrication

The square-shaped disk array on aluminum surface designed for plasmonic structural color printing is schematically illustrated in Fig. 1(a). In order to vary the optical response of the

Optics EXPRESS

designed disk arrays in the visible spectrum, the geometrical parameters of the disk etching depth (*d*), disk width (*w*) and the unit cell period (*P*) are tuned. First, a 250 nm thick aluminum layer is deposited on a silicon wafer using an electron-beam evaporator at a rate of 12 Å/sec. Then the designed disk arrays are directly milled into the aluminum layer using a focused ion beam (FIB) milling process (FEI Helios Nanolab 600 DualBeam) with a gallium ion current of 9.7 pA and an accelerating voltage of 30 KeV. In order to investigate the effects from geometrical parameters, three groups of disk arrays are fabricated with varying *d*, *w* and *P*, respectively. It is noted that the obtained unit cell period during the ion beam milling process is always consistent with the design, while the etching depth and disk width experience slight deviations from the designed values but still in a reasonable range with ± 15 nm variation. After the ion beam milling process, as shown in Figs. 1(b)-1(d), the top width of the square disk is smaller than the bottom width and thus there is a tapered angle of 83° for the disk sidewall. Optical transmission of the designed structure will be effectively blocked due to the limited penetration depth in the thick aluminum layer for incident light in the visible range.

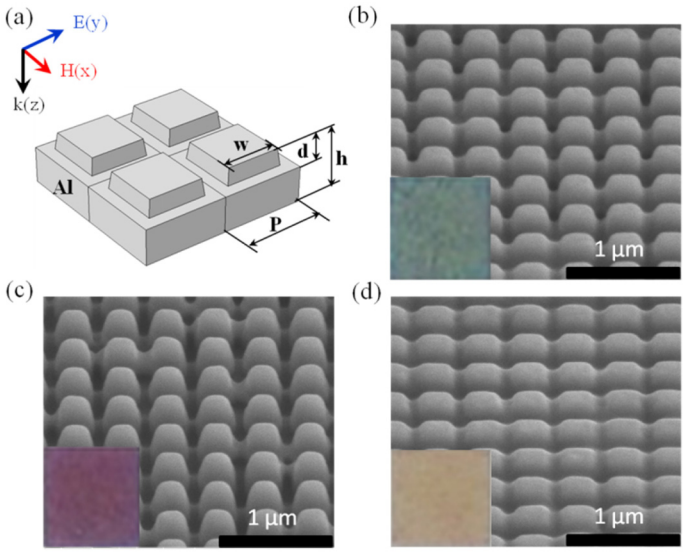

Fig. 1. (a) Schematic of square-shaped disk array on aluminum surface. (b-d) SEM images of square-shaped disk arrays fabricated on h = 250 nm thick aluminum film with different geometric parameters of (b) P = 400 nm, d = 135 nm, w = 245 nm, (c) P = 400 nm, d = 227 nm, w = 200 nm, and (d) P = 400 nm, d = 82 nm, w = 245 nm. Insets: Optical reflection microscope images of 20 × 20 μm^2 disk arrays. Scale bars: 1 μm.

3. Results of experimental characterization and numerical simulation

The optical reflection spectra from the fabricated square-shaped disk arrays are characterized within the visible range (400 ~800 nm) by utilizing an optical spectrometer (LR1, ASEQ instruments). Optical reflection spectrum and the corresponding optical reflection microscope image are collected in the bright field from each fabricated disk array with an area of 20 × 20 μm^2. Figures 1(b)-1(d) show SEM images of three representative disk arrays with different geometrical parameters. The insets display the measured bright-field optical microscope images of these disk arrays, showing three prime colors belonging to the Cyan-Magenta-Yellow (CMY) color model.

Optics EXPRESS

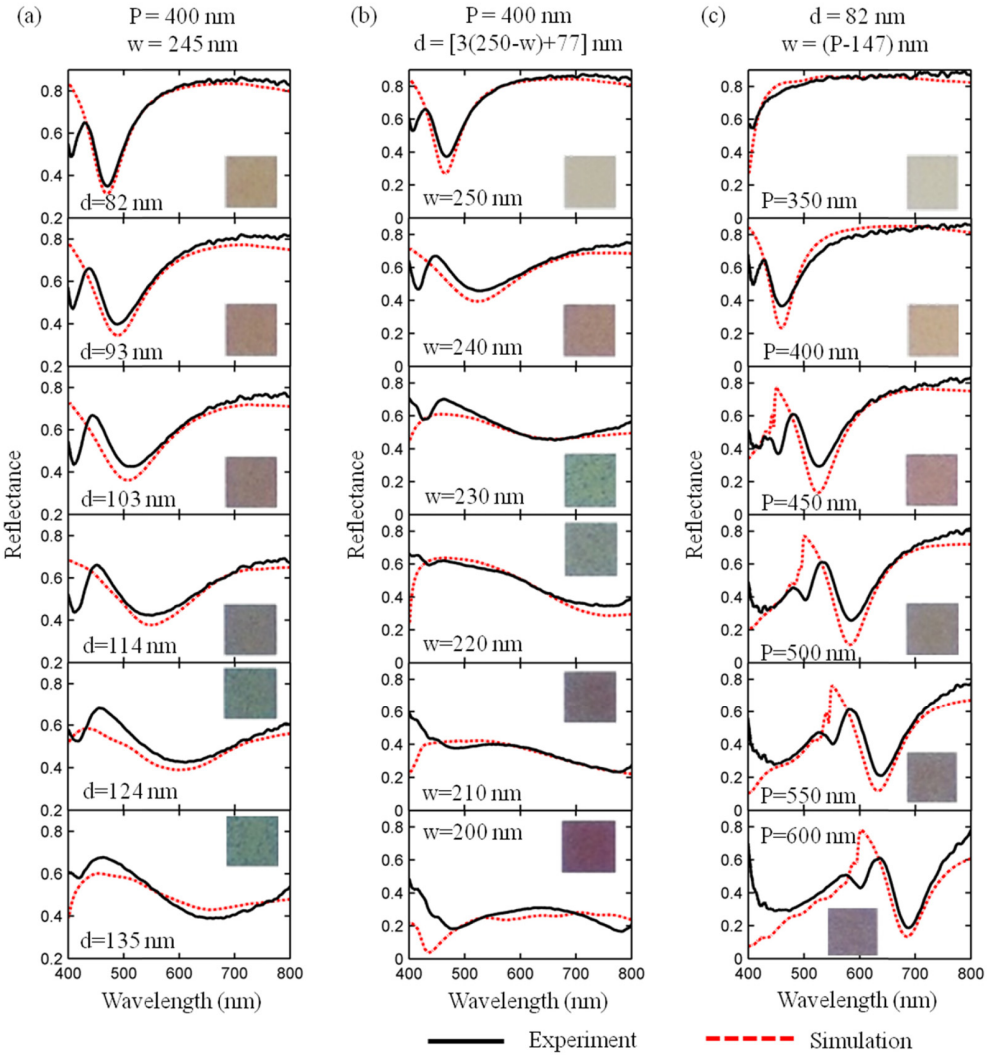

Fig. 2. Measured (black solid line) and simulated (red dashed line) optical reflection spectra of three groups of disk array samples (a) by varying disk etching depth d from 82 nm to 135 nm with constant P = 400 nm and w = 245 nm, (b) by changing disk width w from 250 nm to 200 nm with constant P = 400 nm and d as a function of w, and (c) by changing period P from 350 nm to 600 nm with constant d = 82 nm and P - w = 147 nm. Insets show the optical reflection microscope images of 20 × 20 μm^2 disk arrays. Normal light incidence is employed.

The effects of varying disk etching depth d, disk width w and unit cell period P for the square-shaped disk arrays on the optical reflection spectra and visible colors are further investigated. The measured optical reflection spectra and bright-field microscope images for three groups of disk arrays with varying d, w and P are shown in Fig. 2. In Fig. 2(a), the measured and simulated reflection spectra for disk arrays with varying d exhibit a red-shifted plasmonic resonance and a broader resonance dip as d is increased from 82 nm to 135 nm while w = 245 nm and P = 400 nm are constant. The colors of the microscope images also change accordingly. As shown in Fig. 2(b), a similar optical response is observed for disk arrays with reduced w from 250 nm to 200 nm and constant P = 400 nm. It is noted that d will depend on w during the FIB process due to the variation of ion beam exposure area, giving a rough expression of d = [3(250-w) + 77] nm. Especially for the w = 200 nm case, a broad absorption band is obtained due to both the aluminum loss in the visible spectrum [17, 30, 40,

Optics EXPRESS

41] and the excitation of gap plasmon modes [42, 43]. It is indicated that the obtained visible color range is dependent on both disk etching depth *d* and disk width *w* with a constant unit cell period *P*. Moreover, a wider range of color can be realized with simultaneous variation of both *d* and *w*. In addition, Fig. 2(c) displays the results for disk arrays with varying *P* from 350 nm to 600 nm and $w = (P - 147)$ nm at a constant $d = 82$ nm. As both *P* and *w* are increased, the plasmonic resonance gets red-shifted. Numerical simulation results from the Finite Element Method (COMSOL Multiphysics) are also shown in Fig. 2. The geometrical parameters of square-shaped disk arrays used in simulation are measured from the SEM images. A good match between the experimental and simulation results can be found in Fig. 2. In order to understand the relationship between optical reflection spectra and color generation, all the experimental and simulated reflection spectra depicted in Figs. 2(a)-2(c) have been converted as the discrete points in the CIE 1931 xy chromaticity coordinates based on color theory [44] in Figs. 3(a)-3(c), respectively. As the geometrical parameters of *d*, *w* and *P* for disk arrays vary, the chromaticity coordinates evolve in a clockwise fashion close to the achromatic point, demonstrating the capability of aluminum metasurfaces to produce a relative large degree of visible color range tuning.

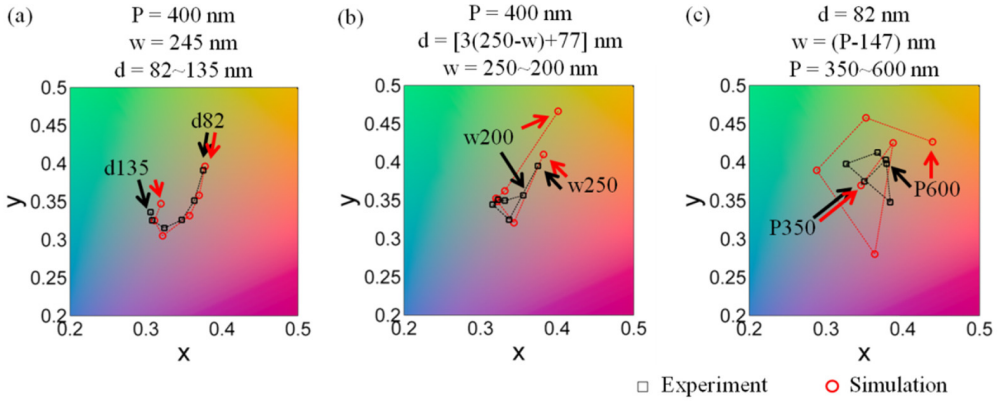

Fig. 3. Measured (black square) and simulated (red circle) results in the CIE 1931 xy chromaticity coordinates for three groups of disk array samples by changing (a) *d*, (b) *w*, and (c) *P*. The reflection spectrum data are obtained from Figs. 2(a)-2(c). The beginning and ending points of parameter variations are labeled for each case.

In order to understand the mechanism of the plasmonic resonance for the square-shaped disk array, optical field distributions at the resonance wavelength of 546 nm are analyzed for one selected sample with $P = 400$ nm, $w = 245$ nm and $d = 114$ nm. As shown in Fig. 4(a), the time-averaged magnetic field (color map) and electric displacement (red arrows) distributions in the *y*-*z* cross section of the designed disk array indicate a strong magnetic dipole resonance [45–47] with enhanced magnetic field concentrated within the air trench surrounded by three aluminum-air interfaces due to the anti-symmetric current flow. At the same time, an electric dipole resonance is also formed on the top aluminum-air interface of the disk. The time-averaged optical power flow distribution in Fig. 4(b) depicts the penetration of light into the aluminum surface layer. The excitation of resonant plasmonic modes will lead to the strong optical absorption for incident light at certain wavelength so that the subtractive color can be observed in the reflection from the disk array sample.

The designed square-shaped disk arrays on aluminum surface can exhibit various visible colors. In Fig. 5, the bright-field microscope images of two color palettes are displayed, where subtractive structural colors are generated from disk arrays with varying geometrical parameters in disk etching depth *d*, disk width *w* and unit cell period *P*. The color palette in Fig. 5(a) includes the disk arrays with constant $P = 400$ nm but varying *w* and *d*, where the dimensions are measured from the SEM images. While the color palette in Fig. 5(b) has the

Optics EXPRESS

disk arrays with a certain P in each row changing from 360 nm to 500 nm and varying w and d. An etching depth beyond the total thickness of the aluminum layer is also obtained experimentally, forming an aluminum-silicon two-layer post array on the silicon substrate. The absorption of incident light is further enhanced by the plasmonic resonance from the two-layer post as well as the optical loss in the silicon substrate. As a result, dark colors can be realized at the upper-right corner of the color palette in Fig. 5(a) and the right columns of the color palette in Fig. 5(b). The wide range of colors achieved with the designed aluminum metasurfaces can be used for structural color printing applications. A micrometer scale plasmonic printed copy [Fig. 6(b)] of a landscape painting we drew [Fig. 6(a)] is fabricated according to the color palettes in Fig. 5(a), where the original image features and colors are successfully reproduced. The SEM images of the fabricated plasmonic painting are shown in Figs. 6(c)-6(e).

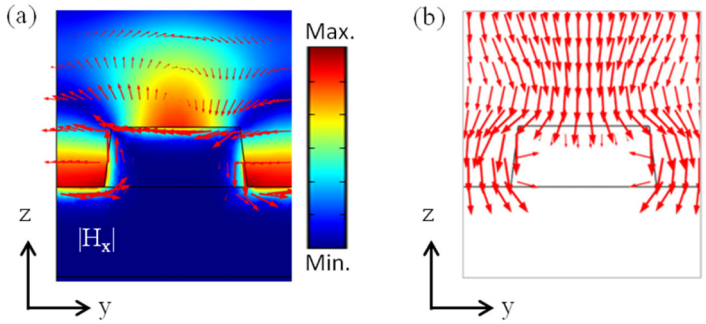

Fig. 4. (a) Cross section of the time-averaged magnetic field (color map) and electric displacement (red arrows) distributions for a selected disk array (with P = 400 nm, w = 245 nm and d = 114 nm) at the resonance wavelength. (b) Cross section of the time-averaged optical power flow vector distribution.

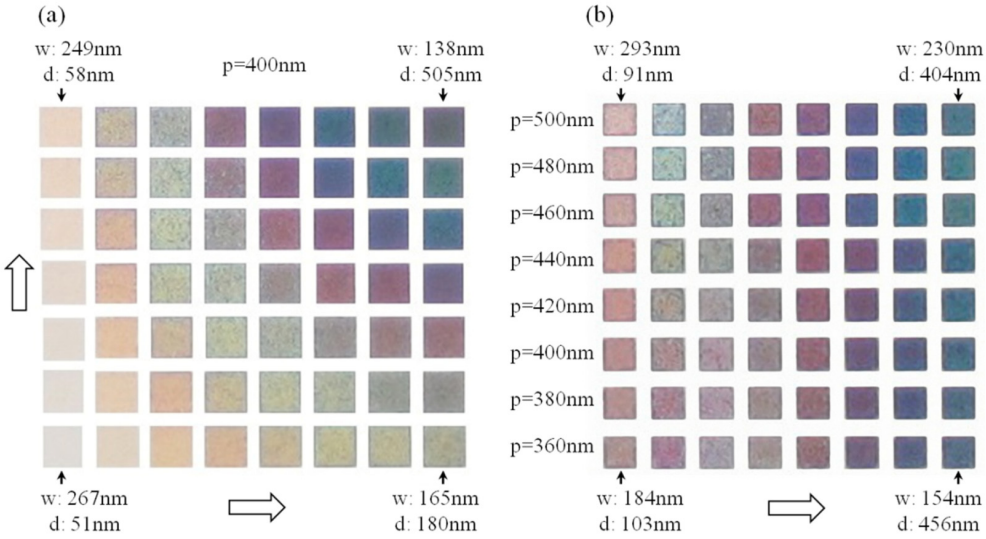

Fig. 5. Color palettes generated from square-shaped disk arrays with varying disk etching depth d, disk width w and unit cell period P. (a) Color palette with constant P = 400 nm but varying w from 267 nm to 138 nm and d from 51 nm to 505 nm. Each fabricated disk array has an area of 15 × 15 μm^2. (b) Color palette with a certain P in each row changing from 360 nm to 500 nm and varying w from 293 nm to 154 nm and d from 91 nm to 456 nm. Each fabricated disk array has an area of 10 × 10 μm^2. The dimensions are measured from the SEM images.

Optics EXPRESS

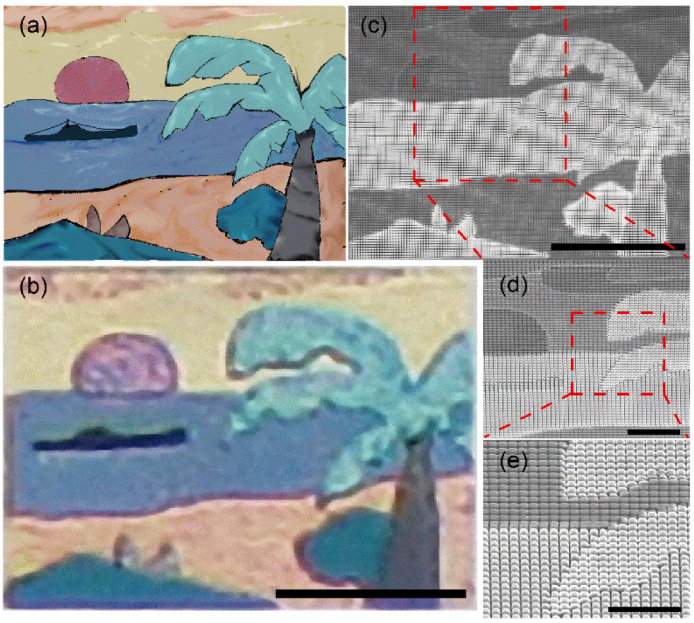

Fig. 6. (a) Original landscape painting with different colors. (b) The measured bright-field optical microscope image of the plasmonic painting with size of 50 μm by 35 μm. (c) SEM image of the fabricated plasmonic painting with various disk array patterns. (d) SEM image of the area outlined in panel (c). (e) SEM image of the area outlined in panel (d). Both SEM images in panels (d) and (e) are tilted with an angle of 52° to show clear three-dimensional disk array structures. Scale bars: 20 μm in (b) and (c), 5 μm in (d), and 3 μm in (e).

4. Incident angle dependence of optical response

By considering the realistic situation for structural color printing applications, the incident angle dependence and polarization dependence of the optical spectral response are investigated in simulation for one designed square-shaped disk array with P = 400 nm, w = 245 nm and d = 114 nm. The calculated TE (electric field parallel to y axis) and TM (magnetic field parallel to y axis) polarized optical reflection spectra with varying incident angle from 0° to 80° are plotted in Figs. 7(a) and 7(b), respectively. Based on color theory [44], the TE and TM polarized reflection spectra are also converted into the chromaticity coordinates as a function of the incident angle from 0° to 80° with a 10° step, as shown in Fig. 7(c). For TE polarization, the plasmonic resonance gives a shallow reflection dip around the wavelength of 550 nm near the 0° incident angle, showing the magenta color. As the incident angle is close to 10° or 80°, there are sharp reflection dips around the wavelength of 450 nm so that the yellow color is presented. When the incident angle is located between 20° and 70°, the reflection spectra have the similar shape and display strong broadband absorption within the wavelength range from 400 nm to 600 nm, which results in the slightly changed orange color. As shown in Fig. 7(c), for TE polarization the chromaticity coordinates vary in the anticlockwise direction as the incident angle is increased from 10° to 80°. While for TM polarization, once the incident angle is larger than 0°, strong optical absorption with varying bandwidth starting from the wavelength of 400 nm is observed. Such absorption bandwidth almost linearly extends into the longer wavelength as the incident angle is increased and the Fano-like features show up in the reflection spectra at the long wavelength edge of the absorption band. The incident angle dependent reflection spectra indicate that the excitation of plasmonic modes are relevant to the grating coupling [22, 34, 48]. As shown in

Optics EXPRESS

Fig. 7(c), for TM polarization the chromaticity coordinates change in the clockwise direction as the incident angle is increased from 10° to 80°, and the color varies from yellow and orange to black. Note that for high incident angles above 60°, the chromaticity coordinates are very close to the achromatic point and the black color will be obtained due to the strong absorption in the whole visible spectrum range.

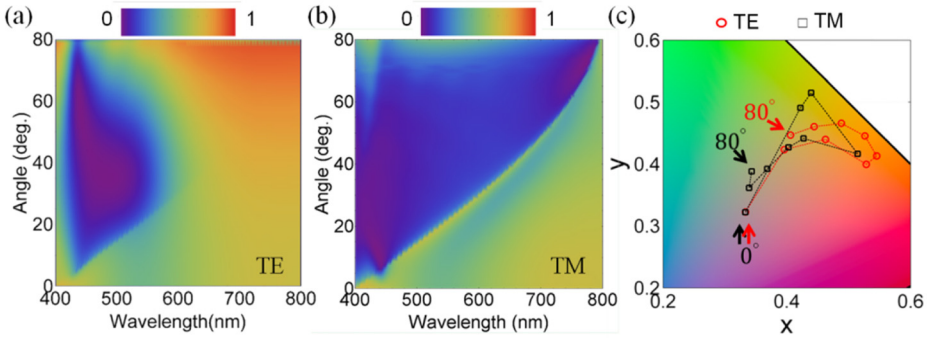

Fig. 7. Simulated incident angle dependent (a) TE and (b) TM polarized optical reflection spectra for a selected disk array (with P = 400 nm, w = 245 nm and d = 114 nm). (c) Incident angle resolved chromaticity coordinates calculated from the reflection spectra for TE (red circle) and TM (black square) polarizations.

5. Conclusion

In summary, we have demonstrated an all-metal structural color printing platform based on aluminum plasmonic metasurfaces with high resolution and high color performance using a simple, one-step focused ion beam milling process on aluminum surface. A wide range of visible colors has been achieved with the plasmonic metasurfaces by varying the geometrical parameters of square-shaped disk arrays including the disk etching depth, the disk width and the unit cell period. The subtractive colors are obtained from the reflection spectra due to the excitation of plasmonic electric and magnetic dipole resonances. The reproduced microscale landscape painting shows the feasibility and flexibility of all-metal plasmonic metasurfaces used for color printing applications. The demonstrated aluminum plasmonic metasurfaces for structural color printing are well-suited for applications such as microscale imaging, information storage, anti-counterfeit tagging and security marking.

Funding

Office of Naval Research (ONR) (N00014-16-1-2408); National Science Foundation (NSF) (DMR-1552871, CBET-1402743); U.S. Department of Energy (DE-AC02-06CH11357).

Acknowledgments

The authors acknowledge the facility support from the Materials Research Center at Missouri S&T. This work was performed, in part, at the Center for Nanoscale Materials, a U.S. Department of Energy, Office of Science, Office of Basic Energy Sciences User Facility under Contract No. DE-AC02-06CH11357.